

See discussions, stats, and author profiles for this publication at: <https://www.researchgate.net/publication/231641167>

# Synthesis and Characterization of Pt(0) Nanoparticles in Imidazolium Ionic Liquids

ARTICLE *in* THE JOURNAL OF PHYSICAL CHEMISTRY B · JUNE 2006

Impact Factor: 3.3 · DOI: 10.1021/jp0623037 · Source: PubMed

---

CITATIONS

143

READS

100

## 6 AUTHORS, INCLUDING:



Giovanna Machado

Centro de Tecnologias Estrategicas do Norde...

51 PUBLICATIONS 1,918 CITATIONS

[SEE PROFILE](#)



Sergio Ribeiro Teixeira

Universidade Federal do Rio Grande do Sul

51 PUBLICATIONS 2,053 CITATIONS

[SEE PROFILE](#)



Jairton Dupont

University of Nottingham

364 PUBLICATIONS 16,049 CITATIONS

[SEE PROFILE](#)

## Synthesis and Characterization of Pt(0) Nanoparticles in Imidazolium Ionic Liquids

Carla W. Scheeren,<sup>†</sup> Giovanna Machado,<sup>†</sup> Sergio R. Teixeira,<sup>‡</sup> Jonder Morais,<sup>‡</sup>  
Josiel B. Domingos,<sup>†</sup> and Jairton Dupont\*,<sup>†</sup>

Laboratory of Molecular Catalysis, Instituto de Química-UFRGS, 9500 P.O. Box 15003, 91501-970,  
Porto Alegre, Brazil, and Instituto de Física-UFRGS, P.O. Box 15051, 91501-970, Porto Alegre, Brazil

Received: April 13, 2006; In Final Form: May 13, 2006

The controlled decomposition of  $\text{Pt}_2(\text{dba})_3$  ( $\text{dba} = \text{dibenzylideneacetone}$ ) dispersed in 1-*n*-butyl-3-methylimidazolium tetrafluoroborate ( $\text{BMI}.\text{BF}_4^-$ ) and hexafluorophosphate ( $\text{BMI}.\text{PF}_6^-$ ) ionic liquids in the presence of cyclohexene by molecular hydrogen produces Pt(0) nanoparticles. The formation of these nanoparticles follows the two-step [ $\text{A} \rightarrow \text{B}$ ,  $\text{A} + \text{B} \rightarrow 2\text{B}$  ( $k_1, k_2$ )] autocatalytic mechanism. The catalytic activity in the hydrogenation of cyclohexene is influenced by the nature of the anion rather than the mean-diameter of the nanoparticles. Thus, higher catalytic activity was obtained with Pt(0) dispersed in  $\text{BMI}.\text{BF}_4^-$  containing the less coordinating anion although these nanoparticles possess a larger mean diameter (3.4 nm) than those obtained in  $\text{BMI}.\text{PF}_6^-$  (2.3 nm). Similar mean diameter values were estimated from in situ XRD and SAXS. XPS analyses clearly show the interactions of the ionic liquid with the metal surface demonstrating the formation of an ionic liquid protective layer surrounding the platinum nanoparticles. SAXS analysis indicated the formation of a semi-organized ionic liquid layer surrounding the metal particles with an extended molecular length of around 2.8 nm in  $\text{BMI}.\text{BF}_4^-$  and 3.3 nm in  $\text{BMI}.\text{PF}_6^-$ .

### Introduction

The use of water or organic solvent stabilizing agents such as surfactants, polymers, quaternary ammonium salts, and polyoxoanions is one of the most current and used approaches for the stabilization of soluble transition-metal nanoparticles.<sup>1–3</sup> Indeed, the advent of these stable metallic particles, which are finely dispersed in organic solvents or in water has enabled the development of one-phase and two-phase catalytic systems for various reactions that operate under relatively mild reaction conditions.<sup>4</sup> The catalytic activity and selectivity of soluble-metal-particle catalysts depends not only on the relative abundance of different types of active sites but also on the concentration and type of stabilizers present in the medium.<sup>5</sup> For example, the catalytic activity of iridium nanoparticles is extremely sensitive to the nature of the capping ligand and ligand coverage. Thus, good capping ligands—that stabilize robust nanocrystals with very narrow size distributions—are almost inactive catalysts for the hydrogenation of olefins.<sup>6</sup> Quaternary ammonium salts are one of the most popular and investigated classes of stabilizing agents for soluble transition-metal nanoparticle catalysts. It is assumed that the stabilization in these cases is due to the positive charge on the metal surface, which is ultimately induced by the adsorption of the anions onto the coordinative unsaturated, electron-deficient, and initially neutral metal surface.<sup>7</sup> Not surprisingly, the stability and catalytic properties of these soluble nanoparticles are strongly dependent on the nature of the anion. For example, it was recently demonstrated that the catalytic properties of Rh nanoparticles are strongly influenced by the nature of the N-containing surfactant counteranion.<sup>8</sup>

We<sup>9–20</sup> and others<sup>21–29</sup> have recently reported that imidazolium ionic liquids (ILs) are an interesting medium for the formation and stabilization of catalytically active transition-metal nanoparticles. The high catalytic activity probably results from the presence of highly undercoordinated atoms on the metal surface due to the loosely supported nanoparticles by the IL. The intrinsic high charge of imidazolium salts, which creates an electrostatic colloid-type protection (DLVO-type stabilization)<sup>30</sup> for the transition-metal nanoparticles similar to those proposed for quaternary ammonium salts,<sup>31–33</sup> may be, as the first approximation,<sup>34</sup> adequate for the description of the stabilizing effect. However, imidazolium salts differ in various aspects from classical quaternary ammonium salts or even molten salts. Imidazolium ILs possess preorganized structures through mainly hydrogen bonds<sup>35,36</sup> that induce structural directionality in opposition to classical salts in which the aggregates display mainly charge-ordering structures.<sup>37</sup> Imidazolium ILs form an extended hydrogen bond and  $\pi-\pi$  stacking (involving the imidazolium rings) network in the liquid state and are consequently highly structured, that is, they can be described as “supramolecular” fluids.<sup>35,38</sup> This is one of the special qualities of imidazolium ILs that differentiates them from the classical ion aggregates of which ion pairs and ion triplets are widely recognized examples.<sup>39</sup> This structural organization of imidazolium ILs functions as an “entropic driver” for spontaneous, well-defined, and extended ordering of nanoscale structures.<sup>40</sup> Therefore, the unique combination of adaptability toward other molecules and phases associated with the strong H-bond-driven fluid structure makes imidazolium ILs “templates” for the formation of nanostructures. Moreover, it is also possible that imidazolium-based ILs may form surface-attached carbenes,<sup>41</sup> at least as transient species, and may also be responsible for the stabilization of zero-valent transition-metal nanoparticles in these fluids.<sup>42</sup> It is evident that a knowledge of the mechanism of formation, the interaction of the ionic liquid

\* To whom correspondence should be addressed. E-mail: dupont@iq.ufrgs.br.

<sup>†</sup> Instituto de Química-UFRGS.

<sup>‡</sup> Instituto de Física-UFRGS.

with the nanoparticles, and how this leads to the stabilization of the nanoparticles without losing their catalytic properties can yield important information for the design and synthesis of stable nanoparticles. In this respect, we have reported that the controlled decomposition of the organometallic Pt(0) precursor  $\text{Pt}_2(\text{dba})_3$ <sup>43–46</sup> in 1-*n*-butyl-3-methylimidazolium hexafluorophosphate (BMI.PF<sub>6</sub>) IL yields stable and catalytically active Pt(0) nanoparticles with a mean diameter of 2.3 nm.<sup>17</sup> Moreover, we were able to observe by TEM contrast density fluctuations around the metal nanoparticles in the IL, and different thicknesses of mass density between the IL and crystalline structures. This mass densities difference is an indication of the effective interaction between the IL and the metal nanoparticles. We wish to disclose herein full details on the kinetics of formation of Pt(0) nanoparticles and a study of their structure and morphology by means of X-ray diffraction (XRD), transmission electron microscopy (TEM), X-ray photoelectron spectroscopy (XPS), and small-angle X-ray scattering (SAXS) obtained from the controlled decomposition of  $\text{Pt}_2(\text{dba})_3$  in hydrophobic and hydrophilic ILs.

## Experimental Section

**General.** All reactions involving platinum compounds were carried out under an argon atmosphere in oven-dried Schlenk tubes.  $\text{Pt}_2(\text{dba})_3$  was prepared according to literature procedures.<sup>47</sup> The halide-free BMI.PF<sub>6</sub>,<sup>48</sup> BMI.BF<sub>4</sub>, and BMI.CF<sub>3</sub>SO<sub>3</sub><sup>49</sup> ILs were prepared according to a known procedure and dried over molecular sieves (4 Å), and their purity was checked by <sup>1</sup>H NMR spectra using the intensity of the <sup>13</sup>C satellites of the imidazolium *N*-methyl group as an internal standard.<sup>50</sup> Solvents, alkenes, and arenes were dried with the appropriate drying agents and distilled under argon prior to use. All other chemicals were purchased from commercial sources and used without further purification. NMR spectra were recorded on a Varian Inova 300 spectrometer. Infrared spectra were performed on a Bomem B-102 spectrometer. Mass spectra were obtained using a GC/MS Shimatzu QP-5050 (EI, 70 eV). Gas chromatography analysis was performed with a Hewlett-Packard-5890 gas chromatograph with an FID and a 30 m capillary column with a dimethylpolysiloxane stationary phase. SAXS analyses were performed at the D11A SAXS beam line of the Brazilian Synchrotron Light Laboratory (LNLS).

XRD analyses were performed on a SIEMENS D500 diffractometer using Bragg–Brentano geometry with a curved graphite crystal as the monochromator. TEM was obtained using a JEOL JEM2010 microscope operating at 200 kV and a JEOL JEM1200ExII operating at 100 kV. A 20 μm objective aperture and slightly under focused ( $\Delta f \approx -300$  nm) objective lens were used to obtain the bright field TEM images.

The nanoparticle formation and hydrogenation reactions were carried out in a modified Fischer–Porter bottle immersed in a silicone oil bath and connected to a hydrogen tank. The temperature was maintained at 75 °C by a hot-stirring plate connected to a digital controller (ETS-D4 IKA). A deliberated stirring of 800 rpm was used (no ionic catalytic solution projection was observed). The fall in the hydrogen pressure in the tank was monitored with a pressure transducer interfaced through a Novus converter to a PC and the data workup via Microcal Origin 5.0.

**Kinetic Data Treatment.** The kinetic data for cyclohexene hydrogenation were fitted using the analytic eq 6 (see later) with Microcal Origin 5.0. The actual rate constants obtained from the fitting for the autocatalytic growth ( $A + B \rightarrow 2B$ ,  $k_{2\text{obs}}$ ) were corrected considering the reaction stoichiometry,

multiplying  $k_{2\text{obs}}$  by the substrate/catalyst molar ratio, to obtain the reported rate constants,  $k_2$  (for further details on these fitting procedures see elsewhere).<sup>51–54</sup>

**Preparation and Isolation of Pt(0) Nanoparticles.** In a typical experiment, to a Fischer–Porter bottle containing BMI.PF<sub>6</sub> (1 mL) or BMI.BF<sub>4</sub> (1 mL) or BMI.CF<sub>3</sub>SO<sub>3</sub> (1 mL) was added  $\text{Pt}_2(\text{dba})_3$  (30 mg, 0.02 mmol), which was stirred at room temperature for 15 min resulting in a violet solution. The system was heated to 75 °C and hydrogen (4 bar) was admitted. After stirring for 1.5 h, a black “solution” was obtained. This solution was washed with dichloromethane (3 × 15 mL), and the Pt(0) nanoparticles were isolated by centrifugation (3500 rpm) for 3 min and washed with acetone (3 × 15 mL) and dried under reduced pressure. The Pt(0) samples thus obtained were prepared for TEM, XRD, XPS, and SAXS analysis and for catalytic experiments.

**In situ Preparation of Nanoscale Pt(0) Particles and Cyclohexene Hydrogenation.** In a typical experiment, to a Fischer–Porter bottle containing BMI.PF<sub>6</sub> (1 mL) or BMI.BF<sub>4</sub> (1 mL) or BMI.CF<sub>3</sub>SO<sub>3</sub> (1 mL) was added  $\text{Pt}_2(\text{dba})_3$  (30 mg, 0.02 mmol) and cyclohexene (11 mg, 0.02 mmol). The system was heated to 75 °C under hydrogen (6 bar). A drop of these Pt(0) samples in the ILs were diluted in 1 mL of the ionic liquid, placed in carbon–copper grid, and analyzed by TEM.

**XRD Analysis.** The phase structures of the Pt(0) nanoparticles prepared in ILs BMI.PF<sub>6</sub>, BMI.BF<sub>4</sub>, and BMI.CF<sub>3</sub>SO<sub>3</sub> were characterized by XRD. For the XRD analysis, the nanoparticles were isolated as a fine powder and placed in the sample holder. The XRD experiments were carried out on a SIEMENS D500 diffractometer equipped with a curved graphite crystal using Cu Kα radiation ( $\lambda = 1.5406$  Å). The diffraction data were collected at room temperature in a Bragg–Brentano  $\theta$ – $2\theta$  geometry. The equipment was operated at 40 kV and 20 mA with a scan range between 20° and 90°. The diffractograms were obtained with a constant step,  $\Delta 2\theta = 0.05$ . The indexation of Bragg reflections was obtained by a pseudo-Voigt profile fitting using the FULLPROF code.<sup>55</sup>

**TEM Analysis.** The morphology and the electron diffraction (ED) of the obtained particles were carried out on a JEOL JEM-2010 equipped with an energy-dispersive X-ray spectroscopy (EDS) system and a JEOL JEM-1200 EXII electron microscope operating at accelerating voltages of 200 and 120 kV, respectively. The samples for TEM were prepared by dispersion of the Pt(0) nanoparticles in ILs at room temperature and then collected on a carbon-coated copper grid. The histograms of the nanoparticles size distribution, assuming spherical shape, were obtained from the measurement of about 300 particles and were reproduced in different regions of the Cu grid, found in an arbitrarily chosen area of enlarged micrographs. The HRTEM images were analyzed in Gatan Digital Micrograph Software from which the Fourier transform of images was obtained.

**XPS Analysis.** The photoemission studies were performed using the VG ESCALAB MkII, equipped with a 150 mm hemispherical analyzer and Al Kα Anode X-ray source. The overall resolution was 200 meV. The detection angle of the photoelectrons was 45° with respect to the sample surface. Samples for analysis were prepared by placing the Pt(0) nanoparticles on a carbon-conducting tape.

**SAXS Data Analysis.** The samples of Pt(0) nanoparticles were analyzed using SAXS at room temperature, at the beam line of the Brazilian Synchrotron Light Laboratory (LNLS). The samples (nanoparticles plus IL) were combined immediately for measurement and injected with a needle syringe in the sample chamber. The sample chamber was sealed with Mylar film on

both sides for incident and scattered X-ray. These measurements were taken out in a transmission geometry with  $\lambda = 1.608 \text{ \AA}$ . The time exposure for each sample was around 1200 s, and the distance between the sample and SAXS detection plane was 963.8 mm. The 2D SAXS spectra were obtained using an image plate as a detector.

**SAXS Data Analysis.** The typical SAXS spectra are shown in Figure 1 for a pure IL and Pt(0) plus IL.

The X-ray scattering is experimentally determined as a function of the scattering vector,  $q$ , whose modulus is given by<sup>56</sup>

$$q = (4\pi \sin \theta)/\lambda \quad (1)$$

where  $\lambda$  is the X-ray wavelength (in the present case  $\lambda = 1.608 \text{ \AA}$ ) and  $\theta$  is half the scattering angle ( $2\theta$ ). First of all, the measured raw SAXS data were corrected for parasitic scattering. The background SAXS scattering from the pattern (IL) and primary incident beam was measured from a sample without nanoparticles and then calculated by subtracting the scattering intensities of the pattern from those of the nanoparticles in suspension. After correction of the scattering data by subtraction of the background noise, the analyses were performed using the methods presented by the references.<sup>57–61</sup>

The most common method for determining periodicity is to use Bragg's law in the calculation of a domain spacing from the location of the peak maximum,  $q_m$  in an  $I(q)q^2 \times q$  plot. The position  $q_m$  is related by Bragg's law to the long period correlation,  $L$ , if that correlation exists, by

$$q_m = 2\pi/L \quad (2)$$

The procedure for the long period determination is based on a one-dimensional semicrystalline model comprising disordered and crystalline phase. This model was adopted in this calculation because we have a two-phase system represented by IL (a quasi-disordered phase) and Pt(0) nanoparticles in the crystalline phase.<sup>62</sup> The morphology and shape of the nanoparticles and ILs were verified using this two-phase model, that is, nanocrystals, represented by the Pt(0) nanoparticles, dispersed in the IL. From this model, it was possible to analyze the SAXS scattering curves via a combination of the correlation function,  $\gamma(r)$ , and interface distribution function,  $g(r)$ .<sup>63</sup> The details about the calculus of the nanoparticles with the ILs obtained by means of SAXS techniques have been recently reported for Ir(0) nanoparticles in imidazolium ILs.<sup>64</sup>

The correlation function,  $\gamma(r)$ , is a measure of the electron density in a sample defined as the Fourier transform of the Lorentz-corrected SAXS profile defined by<sup>65–67</sup>

$$\gamma(r) = \frac{\left( \int_0^\infty I(q)q^2 \cos(qr)e^{-\sigma^2 q^2} dq \right)}{Q} \quad (3)$$

The interface distribution function  $g(r)$  is the Fourier transform of the interference function  $G(q)$ .<sup>22</sup> This function is the second derivative of the correlation function  $g(r) = \gamma''(r)$  defined by eq 4, which represents the probability distribution of finding two interfaces (between a nanocrystal and the adjacent IL region at a distance  $r$ ).

$$g(r) = \frac{\partial^2(\gamma(r))}{\partial r^2} = \frac{\left( \int_0^\infty G(q)\cos(qr)e^{-\sigma^2 q^2} dq \right)}{Q} \quad (4)$$

$$G(q) = K - (I(q)q^2)q^2 e^{-\sigma^2 q^2}$$

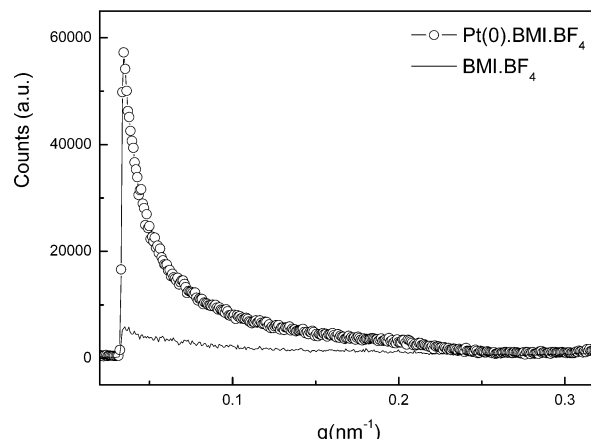


**Figure 1.** Typical SAXS spectra pattern for the pure BMI.BF<sub>4</sub> and Pt(0) dispersed in BMI.BF<sub>4</sub>.

From eq 3, the long period,  $L$ , can be estimated as the position of the first maximum in the correlation function.<sup>66,68</sup>

In the interface distribution function,  $g(r)$ , eq 4, the long period,  $L$  is defined as the first minimum. In both functions ( $\gamma(r)$  and  $g(r)$ ), the long period,  $L$ , is defined as the most probable distance between the centers of gravity between two adjacent IL supramolecular aggregates or between two adjacent nanoparticles dispersed in the IL.<sup>60,63</sup> Note that functions  $\gamma(r)$  and  $g(r)$  are normalized by the invariant scattering  $Q$ . Sophisticated methods involve the calculation of the invariant  $Q$ , which is independent of the size and shape of the structural heterogeneities.  $Q$  represents the electron density difference between the two phases and has been calculated from the area under a Lorentz-corrected scattering curve ( $I(q)q^2 \times q$ ) defined by

$$Q = \int_0^\infty I(q)q^2 dq \quad (5)$$

The application of the correlation and interface distribution function is accepted only in SAXS range data ( $0.1 \text{ nm}^{-1} < q < 2.5 \text{ nm}^{-1}$ ); it must be necessary to extrapolate to both high and low  $q$  values before Fourier transformation. The extrapolation to high  $q$  values was performed with the aid of the Porod law.

## Results and Discussion

**Characterization of the Nanoparticles.** The XRD pattern (Figure 2) of the isolated material confirmed the crystalline Pt(0) and the mean diameter could be estimated from the XRD diffraction pattern by means of the Debye–Scherrer equation calculated from full width at half-maximum (fwhm) of the (111), (200), (220), (311), and (222) planes obtained with Rietveld's refinements.

The most representative reflections of Pt(0) were indexed as face-centered cubic (fcc) with unit cell parameter  $a = 3.9231 \text{ \AA}$ . The simulations of Bragg reflections and Rietveld's refinement were performed with a pseudo-Voigt function using the FULLPROF code.

It is worth pointing out that the use of full width at half-maximum (fwhm) of a peak to estimate the size of crystalline grain by means of the Scherrer equation has serious limitations since it does not take into account the existence of a distribution of sizes and the presence of defects in the crystalline lattice. Therefore, the calculation of average diameter of grain from fwhm of the peak can overestimate the real value since the larger grains give a strong contribution to the intensity, while the smaller grains just enlarge the base of the peak. Moreover, the

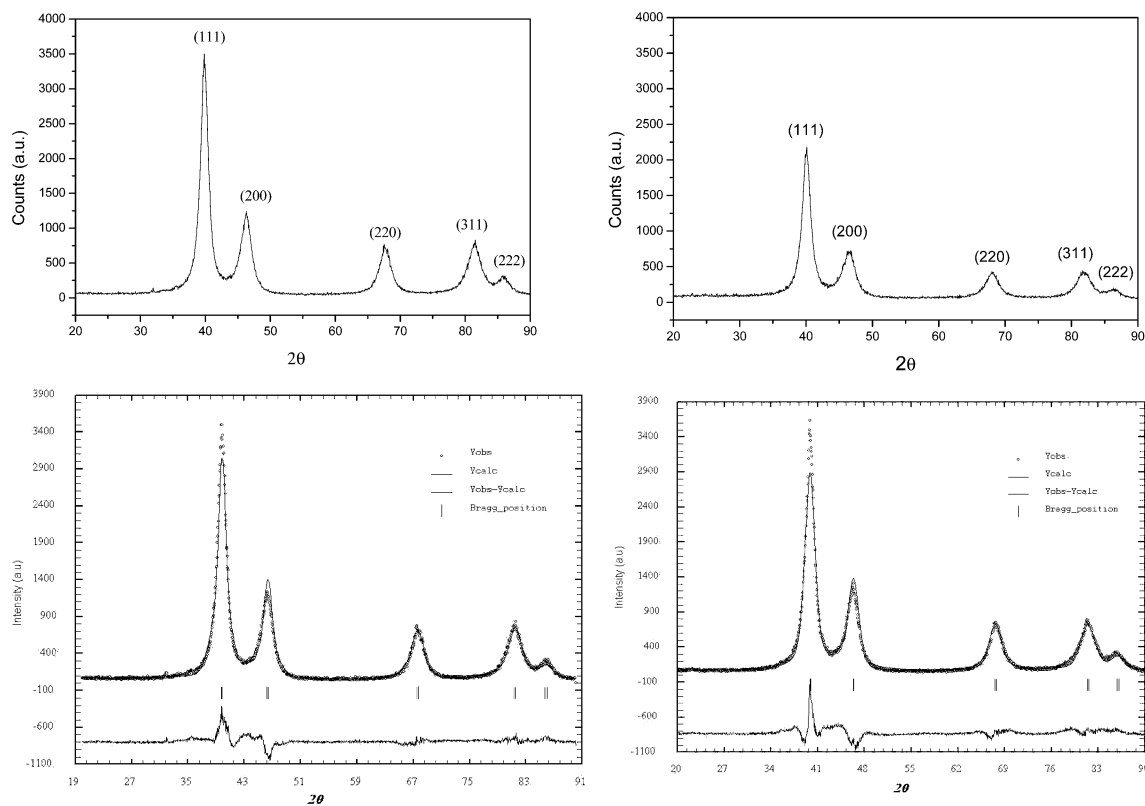


**Figure 2.** X-ray diffraction pattern (top) and Rietveld's refinement (bottom) of the Pt(0) nanoparticles prepared in BMI.PF<sub>6</sub> (left) and in BMI.BF<sub>4</sub> (right).

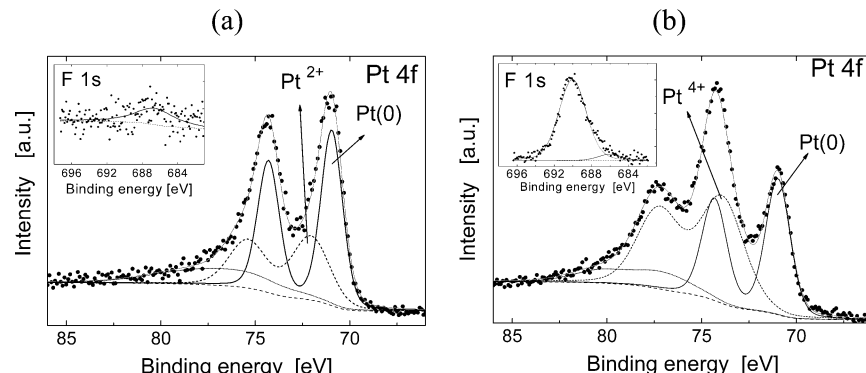


**Figure 3.** X-ray photoelectron spectra of Pt nanoparticles prepared with (a) BMI.BF<sub>4</sub> and (b) BMI.PF<sub>6</sub> showing the Pt 4f region with the fitting results (using Shirley type background). The insets of the figures show the F 1s signal observed for each case.

presence of defects in a significant amount causes an additional enlargement of the diffraction line. Considering this enlargement, the obtained size can be smaller than the real size of the grains. These problems can be minimized by the use of Rietveld's refinement method. Indeed, these discrepancies are confirmed by the values found for the average diameter of the nanoparticles without the structural refinement (3.8 and 5.4 nm) which significantly differs from those found by means of Rietveld's refinement of 2.6 and 3.1 nm for the samples Pt(0).BMI.PF<sub>6</sub> and Pt(0).BMI.BF<sub>4</sub>, respectively. These latter values are much closer to those determined by TEM and SAXS (see later).

The XPS analysis of the isolated nanoparticles showed the presence of platinum, fluorine, and carbon (from the support) for the samples prepared in BMI.BF<sub>4</sub> and BMI.PF<sub>6</sub>. Moreover, in the case of the sample obtained in BMI.PF<sub>6</sub>, there is also a very small contribution of phosphorus. It is clear that the F and P signals indicate that the isolated nanoparticles contain residues

of the ILs. No other impurities were detected within the sensitivity of the technique. Figure 3 shows the XPS signal of the Pt 4f region for both samples.

The Pt 4f spectrum indicates the presence of three chemical states of Pt at the nanoparticle surface with distinct binding energies, and in both samples the contribution due to Pt(0) (Pt<sub>7/2</sub> at 71 eV, thick line) is present. In Figure 3a (BMI.BF<sub>4</sub>), besides the predominant Pt(0) contribution, one notices a component with the Pt<sub>7/2</sub> peak at 72.1 eV (dotted curve), which could be assigned to Pt<sup>2+</sup> and another broad component (Pt<sub>7/2</sub> at 75.7 eV, dashed curve), which could correspond to a mixture of Pt<sup>3+</sup> and Pt<sup>4+</sup> contributions. The F 1s peak observed in this case has a low intensity at about 687 eV.

For the Pt(0) nanoparticles prepared with BMI.PF<sub>6</sub> (Figure 3b), the Pt(0) contribution is less important and another Pt 4f doublet with the Pt<sub>7/2</sub> peak at 74.1 eV (dotted curve) is observed, which could be assigned to Pt<sup>4+</sup>. Again, we notice the presence of a third broad doublet (Pt<sub>7/2</sub> at 75.7 eV, dashed curve)

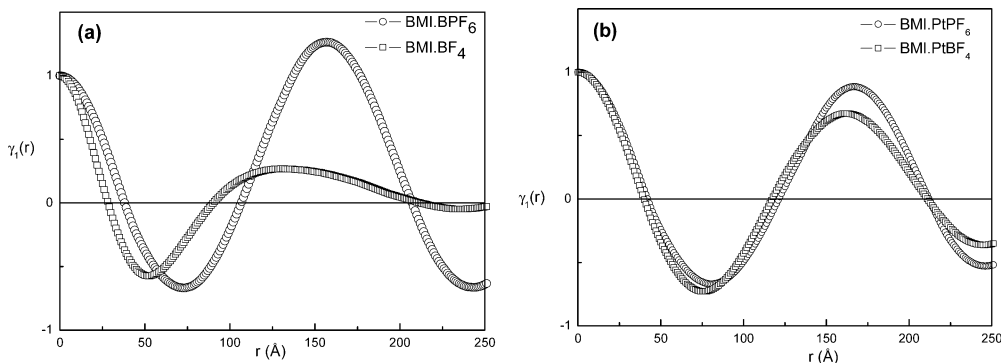


**Figure 4.** Plots of the correlation function for (a) pure ionic liquids and (b) Pt(0) dispersed in the ionic liquids.

corresponding to other chemical bonds at the surface of the nanoparticles. The F 1s signal (at 690 eV) in this sample is quite intense, and we may associate it with the appearance of the Pt<sup>4+</sup> component of the Pt 4f at higher binding energy, as compared with that of the BMI.BF<sub>4</sub> case, due to the abundance of fluorine atoms, which have a higher electronegativity character.

The chemical states that were observed in the Pt 4f signal (Pt(0), Pt<sup>2+</sup>, and Pt<sup>4+</sup>) are related to different bonds between the metallic particles and oxygen and fluorine atoms, forming Pt–F, Pt–O, and Pt–O–F type bonds, whereas the presence of oxygen is probably due to the brief air exposure during the sample preparation process. The measured binding energy values are in accordance with the expected values,<sup>69,70</sup> and the broad peak at higher binding energies could be assigned to mixed bonds. These results are a strong indication of the effective interaction of the IL with the metal surface, which may be responsible for the stabilization of the nanoparticles. More detailed information about the interaction of the nanoparticles with the ILs was obtained from SAXS studies.

Figure 4 shows the correlation function obtained from the SAXS spectra for pure ILs (a) and nanoparticles dispersed in ILs (b). Through the use of the two-phase model,<sup>65–68</sup> it was possible to obtain the diameter of the platinum nanoparticles that are larger than the thickness of the IL layer. As reported earlier, the interface distribution function can be applied to the experimental data for the calculation of the extended molecular lengths of pure ILs.<sup>64</sup> The calculated values for extended molecular lengths of pure ILs of 2.8 nm for BMI.BF<sub>4</sub> and 3.3 nm for BMI.PF<sub>6</sub> are in agreement to those recently reported (2.8 nm for BMI.BF<sub>4</sub> and 4.0 nm for BMI.PF<sub>6</sub>).<sup>64</sup> Interestingly, these values are very close to those estimated by semiempirical calculations (AM1) for the molecular length of [(BMI)<sub>3</sub>(PF<sub>6</sub>)<sub>4</sub>]<sup>-</sup> (3.4 nm) and [(BMI)<sub>2</sub>(BF<sub>4</sub>)<sub>3</sub>]<sup>-</sup> (2.4 nm) supramolecular aggregates.<sup>39</sup>

A considerable increase in  $L$ , with the addition of Pt(0) nanoparticles, was observed for the two ILs studied. This increase was significantly higher for the BF<sub>4</sub> anion, which may have suffered a more ordered structural arrangement, as shown in Figure 4b, where a change of the position of the maximum associated with the long period shifted toward higher  $r$  values. A good agreement was found also for the results derived from correlation and interface distribution functions (see Table 1).

As already reported, this difference may be due to the fact that the PF<sub>6</sub> anion is much larger than the BF<sub>4</sub> anion, thus restricting the cation mobility,<sup>71</sup> hampering the formation of the ordered arrangement in relation to the platinum nanoparticle, despite the greater coordinating ability of the PF<sub>6</sub> anion than the BF<sub>4</sub> anion. This can also be correlated with the calculated

**TABLE 1: Long Period,  $L$ ,  $L_m$ , and  $L_M$  Values Obtained by Correlation Function,  $\gamma(r)$  and Interface Distribution Functions,  $g(r)$**

sample	correlation function, $\gamma(r)$		interface distribution functions, $g(r)$	
	$L$ (Å)	$L_m$ (Å)	$L$ (Å)	$L_M$ (Å)
Pt(0).BMI.BF <sub>4</sub>	162	74	160	81
BMI.BF <sub>4</sub>	127	52	122	57
Pt(0).BMI.PF <sub>6</sub>	166	81	167	87
BMI.PF <sub>6</sub>	157	73	151	65

van der Waals volumes, which are 68 and 48 Å<sup>3</sup> for the PF<sub>6</sub> and BF<sub>4</sub> anions, respectively.<sup>72</sup>

The integrated area under the scattering profile, which represents the electron density difference between the crystal (nanoparticle) and IL region, also increased. This increase of the invariant  $Q$  when the Pt(0) nanoparticles are dispersed in the ILs can be interpreted as an enhancement of the structural ordering of the nanoparticles plus ILs. On the other hand, the distance,  $L_m$ , can be determined as twice the position of the first minimum in the correlation function, which is interpreted as the most probable distance between the centers of gravity of a nanocrystal (platinum nanoparticle) and its adjacent IL region (see Figure 5a). In the interface distribution function,  $g(r)$ , eq 4, the first maximum can be estimated as semi-order ionic-liquid-phase thickness represented by  $L_M$  (see Figure 5b). The model shown in Figure 5 considers that the platinum nanoparticles (ordered phase) are surrounded by anionic supramolecular aggregates of the type [(BMI)<sub>x-n</sub>(X)<sub>n</sub>]<sup>m-</sup> (semi-ordered phase).

The subtraction of the calculated  $L_M$  (ionic liquid molecular lengths) of  $L_m$ , estimated as the ordered phase length (nanoparticle plus the ionic liquid) which has been obtained using the interface distribution and correlation function, gave mean diameters of 3.4 and 3.2 nm for the platinum nanoparticles dispersed in BMI.BF<sub>4</sub> and BMI.PF<sub>6</sub>, respectively.<sup>73</sup>

It is important to note that—as was observed for Ir(0) nanoparticles in the same ionic liquids<sup>64</sup>—calculations using the Guinier approximation law at a small-angle region gave inconsistent results. On opposition, the calculations using Porod law gave consistent results since it assumed the presence of two phases: a crystalline phase (nanoparticles) and a semi-ordered phase (IL).<sup>74–76</sup> This clearly indicates that the assumption that transition-metal nanoparticles are simply diluted in the ILs, that is, the ILs behave as a classical organic solvent, cannot be applied in these cases.

The TEM micrographs of the nanoparticles *in situ* in the ILs BMI.PF<sub>6</sub> and BMIBF<sub>4</sub>, respectively, are presented in Figure 6. The particles of Pt(0) were also analyzed by energy dispersion spectrometry (see S1 in the Supporting Information). The values

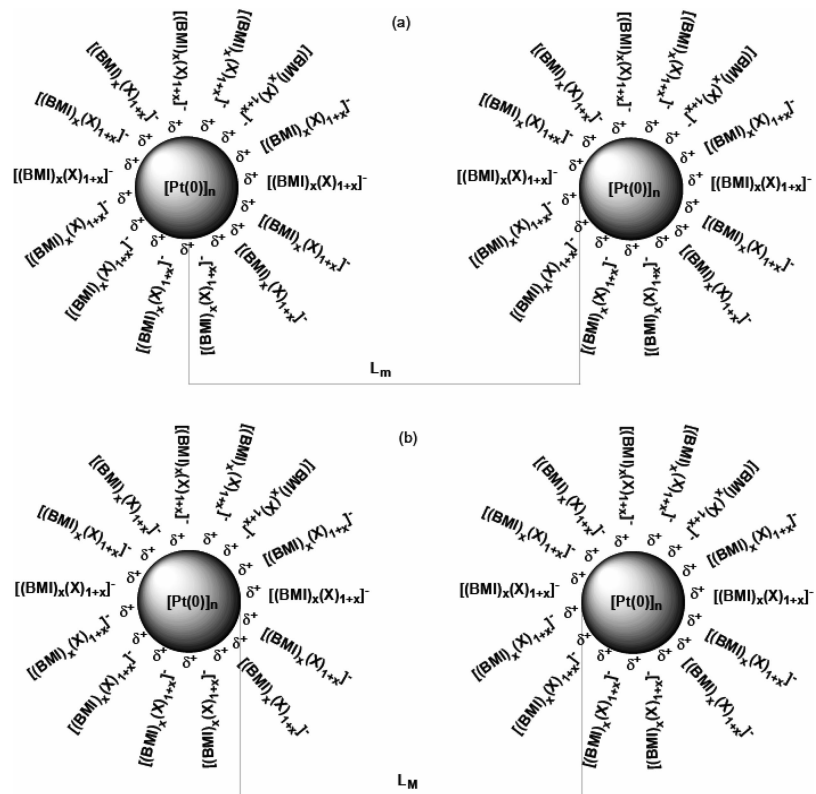


**Figure 5.** Schematic illustration of the proposed two-phase model: (a) corresponds to the correlation function and (b) to the interface distribution function. (a)  $L_m$ , the first minimum, is interpreted as the most probable distance between the center of gravity of a  $Pt(0)$  nanoparticle and its adjacent region. (b)  $L_M$ , the first maximum, can be estimated as disordered ionic-liquid-phase thickness. If  $X = BF_4$ ,  $x = 2$ , and if  $X = PF_6$ ,  $x = 3$ .

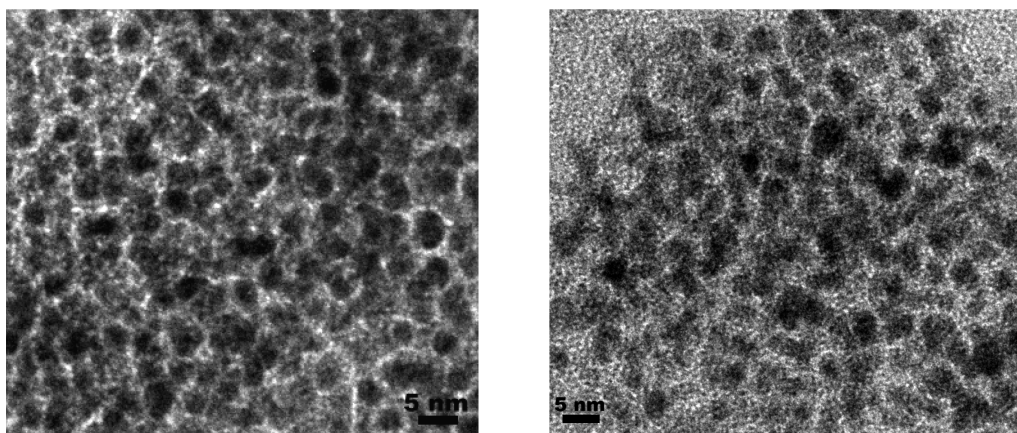


**Figure 6.** TEM micrographs (top) and histograms (bottom) showing the particle size distribution of  $Pt(0)$  prepared in  $BMI.BF_4$  (left) and in  $BMI.PF_6$  (right).

of energy are in agreement with the values of energy for the pattern of  $Pt(0)$ .

Moreover, the crystalline structure of the materials was confirmed by selected area diffraction which shows ring patterns

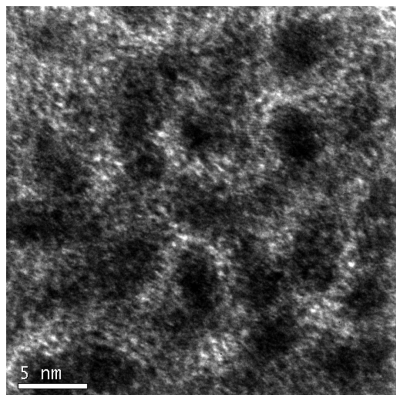


**Figure 7.** TEM micrograph (negative image, under focus) of the Pt(0) in BMI.PF<sub>6</sub> ionic liquid showing the contrast density fluctuation around the metal nanoparticles.

that can be fitted to simulation based on Pt(0) parameters (see S2 in the Supporting Information) as well as by Gatan Digital Micrograph Software from FFT.

Analysis of the micrographs indicate that these Pt(0) nanoparticles display an irregular shape, but evaluating their characteristic diameter, results in a mono modal distribution with an average diameter of 2.3 nm for those prepared in BMI.PF<sub>6</sub> and 3.4 nm for those in BMI.BF<sub>4</sub> estimated from ensembles of 300 particles found in an arbitrarily chosen area of the enlarged micrographs. The histograms of Figure 6 show that particle size distributions can be reasonably well fitted by a Gaussian curve.

The detailed analysis of the nanoparticles of Pt(0) dispersed in the IL BMI.PF<sub>6</sub> shows a rather strong fluctuation of the contrast density (see Figure 7). These fluctuations of contrast density are characteristic of amorphous substances.

The TEM images were compared with those of a pure carbon film and with the images from samples containing only IL. The sample regions containing particles embedded in the IL should not present a high contrast density fluctuation if the surrounding IL were to maintain its liquid features as in the pure liquid observation field. The perimeter and the core of the particle images also show strong contrast density fluctuations under larger under focus conditions, and upon increasing under focus, it becomes difficult to observe, offering strong evidence for the interaction features of the BMI.PF<sub>6</sub> IL with the Pt(0) nanoparticles. The defect in the crystalline lattice was confirmed by HRTEM measurements of the nanoparticles prepared in BMI.BF<sub>4</sub>. The particles that have one twin are shown in the micrograph presented in Figure 8. Note that twin defects are typical for small particles, and the presence of such defects in a significant amount causes an additional enlargement of the diffraction line as observed by Rietveld's refinements. Moreover, these defects are more pronounced in the nanoparticles prepared in BMI.BF<sub>4</sub> than those formed in BMI.PF<sub>6</sub> suggesting that the particle defects depend on the binding abilities of the anions. In this HRTEM image (Figure 8), it was possible, by means of Gatan software, to obtain the Fourier transform from which a lattice spacing of 2.30 and 2.04 Å were calculated corresponding to an experimental error < 5%. These lattice spacings corresponding to the interplanar distances (1 1 1) and (2 0 0) of the Pt(0) are depicted by the arrows in Figure 8 and could be defined as the ⟨0 - 2 2⟩ orientation with respect to the electron beam.

An excellent agreement was found between TEM, SAXS, and XRD methods for determining the mean relative diameters of the nanoparticles in the two ILs. Comparisons of the values obtained with the different techniques are summarized in Table 2.

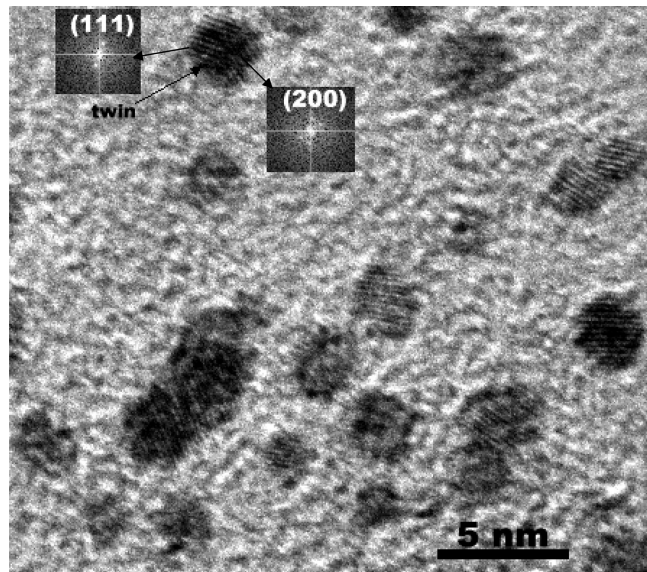


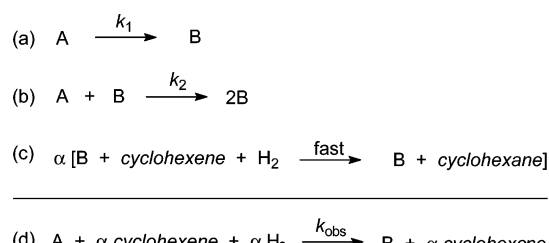
**Figure 8.** Experimental HRTEM images of single twinned platinum nanoparticles in BMI.BF<sub>4</sub>, observing the planar defects and interplanar distance indicated by arrows.

**TABLE 2: Mean Diameter of the Pt Nanoparticles Determined by TEM, SAXS, and XRD**

sample	TEM (nm) <sup>a</sup>	SAXS (nm)	XRD (nm) <sup>b</sup>
Pt(0).BMI.BF <sub>4</sub>	3.4 ± 0.3 (3.4 ± 0.8)	3.4 ± 0.4	3.1 ± 0.4 (5.4 ± 0.7)
Pt(0).BMI.PF <sub>6</sub>	2.3 ± 0.3 (2.4 ± 0.7)	3.2 ± 0.4	2.6 ± 0.4 (3.8 ± 0.6)

<sup>a</sup> Isolated and redispersed nanoparticles and in parentheses mean diameter obtained in situ (see Figure 10). <sup>b</sup> Mean diameter obtained without Rietveld's refinement method in parentheses.

### SCHEME 1



It is also clear that the nanoparticles prepared in BMI.PF<sub>6</sub> that have the stronger binding anion<sup>36</sup> are smaller than those prepared in BMI.BF<sub>4</sub>.

**In situ Investigations of Pt(0) Nanoparticle Formation.** To follow the formation of these Pt(0) nanoparticles in situ, we made use of an indirect method developed by Finke and co-workers.<sup>52</sup> The Pt(0) nanoparticles catalyzed hydrogenation (H<sub>2</sub> uptake) of cyclohexene is used as a reporter reaction via the pseudo-elementary step concept, Scheme 1 (where A is the precatalyst Pt<sub>2</sub>(dba)<sub>3</sub> and B is the catalytically active Pt(0) nanoclusters).

If cyclohexene hydrogenation (step c, Scheme 1) is a fast reaction, on the time scale of steps a and b, it can serve as a reporter reaction for the Pt(0) formation, that is, the kinetics of the overall reaction are those represented only by steps a and b in Scheme 1. Moreover, the sum of all three steps leads to a “kinetically equivalent” elementary step which is related the overall H<sub>2</sub> consumption stoichiometry (cyclohexene) with the formation of Pt(0) nanoparticles, the so-called pseudo-elementary step d (Scheme 1).

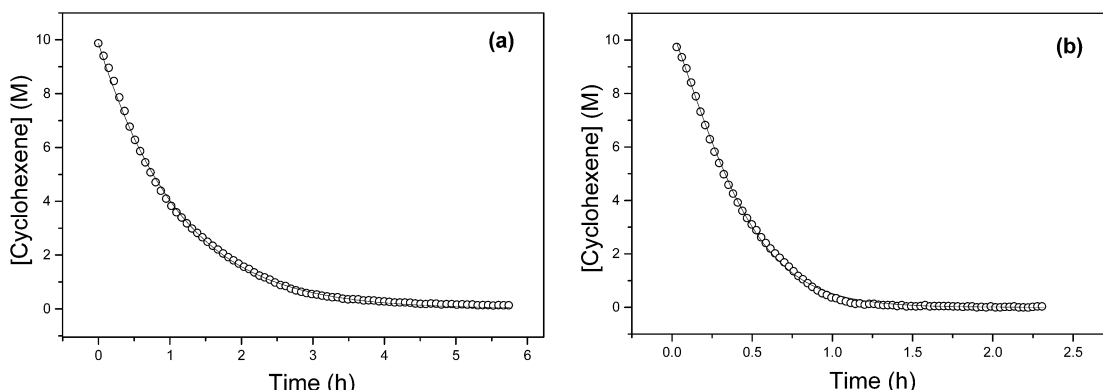


**Figure 9.** Cyclohexene hydrogenation curve with the catalyst precursor  $\text{Pt}_2(\text{dba})_3$  dispersed in (a)  $\text{BMI}.\text{PF}_6$  and (b)  $\text{BMI}.\text{BF}_4$  under 6 atm constant hydrogen pressure at  $75^\circ\text{C}$ . The  $\text{Pt}_2(\text{dba})_3/\text{cyclohexene}$  molar ratio = 250.

**TABLE 3: Rate Constants,  $k_1$  and  $k_2$ , Obtained on the Hydrogenation of Cyclohexene<sup>a</sup> by the Catalyst Precursor  $\text{Pt}_2(\text{dba})_3$  Dispersed in  $\text{BMI}.\text{PF}_6$  and  $\text{BMI}.\text{BF}_4$**

ionic liquid	$k_1 (\text{h}^{-1})$	$k_2 (\text{M}^{-1}\cdot\text{h}^{-1})^b$
$\text{BMI}.\text{PF}_6$	0.86	2.50
$\text{BMI}.\text{BF}_4$	1.34	70.50

<sup>a</sup>  $75^\circ\text{C}$  and under 6 atm of hydrogen (constant pressure). <sup>b</sup> Rate constants obtained considering the substrate/catalyst ratio = 250.

This mechanism is equivalent to the two-step mechanism for transition-metal nanocluster self-assembly, from metal salts under reductive conditions, proposed by Finke<sup>52,54</sup> with one main conceptual difference. Since  $\text{Pt}_2(\text{dba})_3$  is a Pt(0) nanocluster precursor in the zero oxidation state, the first step, as in Scheme 1, must be considered the metal-compound decomposition and not a metal nucleation step as occurs, for example, using a Pt precursor as in an oxidation state different than zero.

The kinetics for the hydrogenation of cyclohexene catalyzed by  $\text{Pt}_2(\text{dba})_3$  dispersed in  $\text{BMI}.\text{PF}_6$  and  $\text{BMI}.\text{BF}_4$  are shown in Figure 9. The kinetic curves above were treated using the pseudo-elementary step and fitted by the following integrated rate equation for metal-compound decomposition ( $\text{A} \rightarrow \text{B}$ ,  $k_1$ ) and autocatalytic nanocluster surface growth ( $\text{A} + \text{B} \rightarrow 2\text{B}$ ,  $k_2$ ). For a more detailed description of the use of a pseudo-elementary step for the treatment of hydrogenation kinetic data and derivatization of the kinetic equations, see elsewhere.<sup>51,52,54</sup>

$$[\text{cyclohexene}]_t =$$

$$\frac{(k_1/k_2) + [\text{cyclohexene}]_0}{1 + \frac{k_1}{k_2[\text{cyclohexene}]_0} \exp^{(k_1+k_2[\text{cyclohexene}]_0)t}} \quad (6)$$

As expected, the kinetic curve of Figure 9 shows no induction period, indicating that the first step, the  $\text{Pt}_2(\text{dba})_3$  decomposition, is fast and the catalyst nanocluster B is readily available at the onset of the hydrogenation reaction. The obtained rate constant values from the fit of Figure 9 are summarized in Table 3.

The kinetic curves shown in Figure 9 can also be fitted by a simple exponential equation, which is possible because the surface growth step ( $k_2$ ) is quite slow when compared with the decomposition step ( $k_1$ )—one must take into consideration the species concentration when comparing first and second-order rate constants—and therefore,  $k_2$  has a very small influence on the global rate for the nanoparticle formation.

These observations are very important when combined with the data from the TEM analysis of the nanoparticles in situ (see Figures 6 and 10). Transmission electron microscopy revealed an average nanoparticle size, after reaction completion, of 3.4

nm in  $\text{BMI}.\text{BF}_4$  and 2.3 nm in  $\text{BMI}.\text{PF}_6$ , corroborating with the idea that agglomeration is not dominant in the formation of these nanoclusters and the small-sized Pt(0) nanoparticles are the true catalyst responsible for the catalytic hydrogenation reaction.

Noteworthy, these mean diameters are very close to those obtained by XRD of the isolated and redispersed Pt(0) nanoparticles (Table 2) in the two ILs.

Moreover, attempts to fit the curve with a mechanism including a third step, the bimolecular aggregation ( $\text{B} + \text{B} \rightarrow \text{C}$ ,  $k_3$ ),<sup>77,78</sup> or with the recently discovered double autocatalytic mechanism,<sup>79,80</sup> which includes a fourth step for the formation of bulk-metal ( $\text{B} + \text{C} \rightarrow 1.5\text{C}$ ,  $k_4$ ), did not converge the fit, which again strongly suggests that agglomeration is not significant in our case. Noteworthy, no metallic platinum was observed in these experiments.

It is also noteworthy that the cyclohexene hydrogenation in  $\text{BMI}.\text{BF}_4$ , in which larger nanoparticles are formed, is much faster than that performed in  $\text{BMI}.\text{PF}_6$  where smaller particles are formed. This is at first glance contradictory since it is expected that smaller nanoparticles should in principle display higher catalytic activity than the larger ones. However, it is most probable that in this case the nanoparticles surface is more exposed since the  $\text{BF}_4^-$  anion is much less coordinating than the  $\text{PF}_6^-$  anion (see XPS analysis).

To verify this hypothesis, the formation of Pt(0) nanoparticles in  $\text{BMI}.\text{CF}_3\text{SO}_3$  IL, which possesses a more strongly binding anion, was also investigated (Figure 11). Indeed, the reaction rate in  $\text{BMI}.\text{CF}_3\text{SO}_3$  is much slower than the reaction performed with the other two ILs. Note that the mean diameter of nanoparticles prepared in  $\text{BMI}.\text{CF}_3\text{SO}_3$  is 3.0 nm (see Supporting Information), that is, very close to that obtained in  $\text{BMI}.\text{BF}_4$ .

Moreover, the nanoparticles prepared in  $\text{BMI}.\text{BF}_4$  were isolated and redispersed in  $\text{BMI}.\text{PF}_6$ , and those isolated from  $\text{BMI}.\text{PF}_6$  were redispersed in  $\text{BMI}.\text{BF}_4$  (Table 4). These nanoparticle dispersions were used in the hydrogenation of 1-hexene, and the reactions performed in the IL containing the more coordinating anion ( $\text{PF}_6^-$ ) are much slower than those performed in  $\text{BMI}.\text{BF}_4$ . Note that the miscibility of 1-hexene is almost identical in both ionic liquids and that the reactions were performed at 6 atm of hydrogen pressure, that is, in conditions where the reaction is not under mass transfer control.<sup>82</sup> This result is another indication that the nanoparticle is surrounded by the anionic species of the ionic liquid.

**Conclusions.** We have demonstrated that the autocatalytic model can be applied for the formation of Pt(0) nanoparticles from the decomposition of  $\text{Pt}_2(\text{dba})_3$  in three different ILs ( $\text{BMI}.\text{PF}_6$ ,  $\text{BMI}.\text{BF}_4$ , and  $\text{BMI}.\text{CF}_3\text{SO}_3$ ). XRD analysis of the

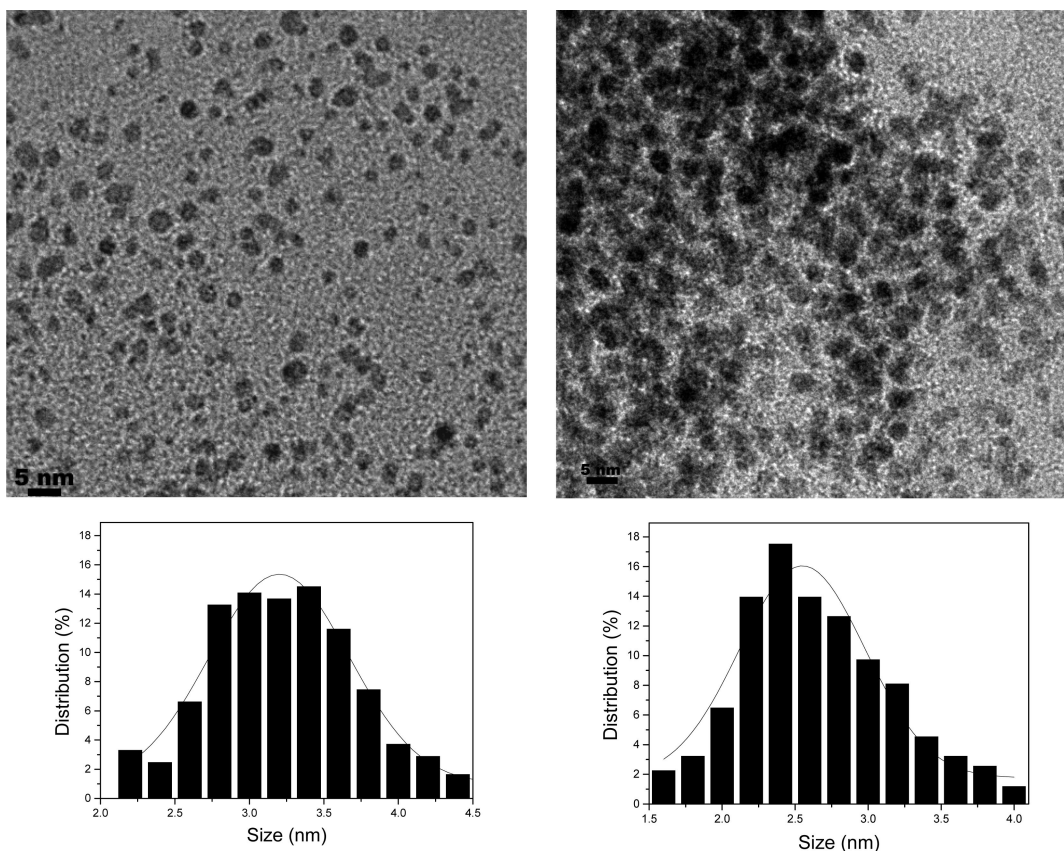


**Figure 10.** In situ TEM micrographs (top) and histograms (bottom) showing the particle size distribution of Pt(0) in BMI.BF<sub>4</sub> (left) and in BMI.PF<sub>6</sub> (right) after the hydrogenation of cyclohexene.

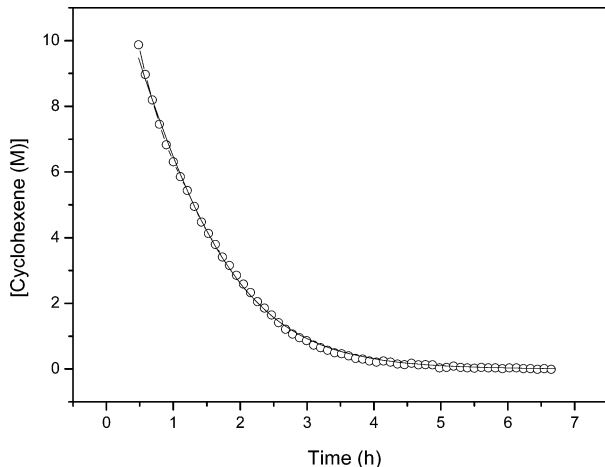


**Figure 11.** Cyclohexene hydrogenation curve with the catalyst precursor Pt<sub>2</sub>(dba)<sub>3</sub> dispersed in BMI.CF<sub>3</sub>SO<sub>3</sub> under 6 atm constant hydrogen pressure at 75 °C. The Pt<sub>2</sub>(dba)<sub>3</sub>/cyclohexene molar ratio = 250 ( $k_1 = 0.53 \text{ h}^{-1}$  and  $k_2 = 11.5 \text{ M}^{-1} \cdot \text{h}^{-1}$ ).

isolated nanoparticles shows that smaller Pt(0) nanoparticles of around 2.3 nm are obtained in ILs containing more coordinating anion (PF<sub>6</sub>) whereas larger particles with 3.4 nm in mean diameter were formed in the IL BMI.BF<sub>4</sub>. XPS analysis clearly demonstrated the formation of an ionic liquid protective layer surrounding the nanoparticle surface. This protective layer is probably composed of semi-organized anionic species present as supramolecular aggregates of the type [(BMI)<sub>x</sub>(X)<sub>x+1</sub>]<sup>-</sup> ( $x = 2$  for X = BF<sub>4</sub> and  $x = 3$  for X = PF<sub>6</sub>) with an extended molecular length of 2.8 nm for BMI.BF<sub>4</sub> and 3.3 nm for BMI.PF<sub>6</sub> as calculated from SAXS data. Moreover, the high catalytic activity observed for the larger nanoparticles in

**TABLE 4: 1-Hexene Hydrogenation by Pt(0) Nanoparticles Isolated from BMI.BF<sub>4</sub> (3.4 nm) and Redispersed in BMI.PF<sub>6</sub> and Those Isolated from BMI.PF<sub>6</sub> (2.3 nm) and Redispersed in BMI.BF<sub>4</sub> at 75 °C under 6 atm of Hydrogen (constant pressure) and 1-hexene/Pt = 250**

entry	Pt(0) medium preparation	Pt(0) size (nm)	reaction medium	TOF (h <sup>-1</sup> ) <sup>a</sup>
1	BMI.BF <sub>4</sub>	3.4 ± 0.3	BMI.PF <sub>6</sub>	404 (1300)
2	BMI.PF <sub>6</sub>	2.3 ± 0.3	BMI.BF <sub>4</sub>	1000 (2380)

<sup>a</sup> Turnover frequency = mol(1-hexene)/mol(Pt<sub>2</sub>(dba)<sub>3</sub>)·h and in parentheses the corrected turnover frequency considering only the exposed atoms on the nanoparticle surface (3.4 nm, 32%, and 2.3 nm, 42%) using the magic number approach.<sup>81</sup>

BMI.BF<sub>4</sub> can be ascribed to the presence of highly uncoordinated atoms compared with those reactions performed in ILs containing more coordinating anions (PF<sub>6</sub> and CF<sub>3</sub>SO<sub>3</sub>). Moreover, the IL anion also plays an important role in the shape of nanoparticles formation, that is, more imperfect nanoparticles are formed in processes performed in ILs containing less coordinating anion (BF<sub>4</sub>) than those synthesized in ILs containing the PF<sub>6</sub> and CF<sub>3</sub>SO<sub>3</sub> anions.

**Acknowledgment.** Thanks are due to the following agencies: CNPq, CAPES, CT-PETRO, FAPERGS, and TWAS for partial financial support. We also acknowledge the staff of LNLS (Project D11A-SAXS, 2003) for technical assistance. We also thank Prof. R. G. Finke and E. E. Finney (Colorado State University) for help in the curve fitting and for the use of the MacKinetic program.

**Supporting Information Available:** Energy dispersion spectrometry and electron diffraction micrograph of Pt(0) nanoparticles prepared in BMI.PF<sub>6</sub> and X-ray diffraction and

TEM micrographs showing the particle size distribution of Pt(0) prepared in BMI.CF<sub>3</sub>SO<sub>3</sub>. This material is available free of charge via the Internet at <http://pubs.acs.org>.

## References and Notes

- (1) Astruc, D.; Lu, F.; Aranzaes, J. R. *Angew. Chem., Int. Ed.* **2005**, *44*, 7852.
- (2) Bonnemann, H.; Richards, R. M. *Eur. J. Inorg. Chem.* **2001**, 2455.
- (3) Finke, R. G.; Ozkar, S. *Coord. Chem. Rev.* **2004**, 248, 135.
- (4) Roucoux, A.; Schulz, J.; Patin, H. *Chem. Rev.* **2002**, *102*, 3757.
- (5) Aiken, J. D.; Finke, R. G. *J. Mol. Catal. A: Chem.* **1999**, *145*, 1.
- (6) Stowell, C. A.; Korgel, B. A. *Nano Lett.* **2005**, *5*, 1203.
- (7) Ozkar, S.; Finke, R. G. *J. Am. Chem. Soc.* **2002**, *124*, 5796.
- (8) Roucoux, A.; Schulz, J.; Patin, H. *Adv. Synth. Catal.* **2003**, *345*, 222.
- (9) Gelesky, M. A.; Umpierre, A. P.; Machado, G.; Correia, R. R. B.; Magno, W. C.; Morais, J.; Ebeling, G.; Dupont, J. *J. Am. Chem. Soc.* **2005**, *127*, 4588.
- (10) Cassol, C. C.; Umpierre, A. P.; Machado, G.; Wolke, S. I.; Dupont, J. *J. Am. Chem. Soc.* **2005**, *127*, 3298.
- (11) Umpierre, A. P.; Machado, G.; Fecher, G. H.; Morais, J.; Dupont, J. *Adv. Synth. Catal.* **2005**, *347*, 1404.
- (12) Fonseca, G. S.; Silveira, E. T.; Gelesky, M. A.; Dupont, J. *Adv. Synth. Catal.* **2005**, *347*, 847.
- (13) Fonseca, G. S.; Scholten, J. D.; Dupont, J. *Synlett* **2004**, 1525.
- (14) Rossi, L. M.; Dupont, J.; Machado, G.; Fichtner, P. F. P.; Radtke, C.; Baumvol, I. J. R.; Teixeira, S. R. *J. Braz. Chem. Soc.* **2004**, *15*, 904.
- (15) Silveira, E. T.; Umpierre, A. P.; Rossi, L. M.; Machado, G.; Morais, J.; Soares, G. V.; Baumvol, I. L. R.; Teixeira, S. R.; Fichtner, P. F. P.; Dupont, J. *Chem.-Eur. J.* **2004**, *10*, 3734.
- (16) Rossi, L. M.; Machado, G.; Fichtner, P. F. P.; Teixeira, S. R.; Dupont, J. *Catal. Lett.* **2004**, *92*, 149.
- (17) Scheeren, C. W.; Machado, G.; Dupont, J.; Fichtner, P. F. P.; Teixeira, S. R. *Inorg. Chem.* **2003**, *42*, 4738.
- (18) Fonseca, G. S.; Umpierre, A. P.; Fichtner, P. F. P.; Teixeira, S. R.; Dupont, J. *Chem.-Eur. J.* **2003**, *9*, 3263.
- (19) Dupont, J.; Fonseca, G. S.; Umpierre, A. P.; Fichtner, P. F. P.; Teixeira, S. R. *J. Am. Chem. Soc.* **2002**, *124*, 4228.
- (20) Bruss, A. J.; Gelesky, M. A.; Machado, G.; Dupont, J. *J. Mol. Catal. A: Chem.* **2006**, *252*, 212.
- (21) Zhao, D.; Fei, Z.; Geldbach Tilmann, J.; Scopelliti, R.; Dyson Paul, J. *J. Am. Chem. Soc.* **2004**, *126*, 15876.
- (22) Calo, V.; Nacci, A.; Monopoli, A.; Montingelli, F. *J. Org. Chem.* **2005**, *70*, 6040.
- (23) Calo, V.; Nacci, A.; Monopoli, A.; Fornaro, A.; Sabbatini, L.; Cioffi, N.; Ditaranto, N. *Organometallics* **2004**, *23*, 5154.
- (24) Calo, V.; Nacci, A.; Monopoli, A.; Laera, S.; Cioffi, N. *J. Org. Chem.* **2003**, *68*, 2929.
- (25) Calo, V.; Nacci, A.; Monopoli, A.; Detomaso, A.; Iliade, P. *Organometallics* **2003**, *22*, 4193.
- (26) Anderson, K.; Cortinas Fernandez, S.; Hardacre, C.; Marr, P. C. *Inorg. Chem. Commun.* **2003**, *7*, 73.
- (27) Huang, J.; Jiang, T.; Han, B.; Gao, H.; Chang, Y.; Zhao, G.; Wu, W. *Chem. Commun.* **2003**, 1654.
- (28) Mu, X. D.; Meng, J. Q.; Li, Z. C.; Kou, Y. *J. Am. Chem. Soc.* **2005**, *127*, 9694.
- (29) Gao, S. Y.; Zhang, H. J.; Wang, X. M.; Mai, W. P.; Peng, C. Y.; Ge, L. H. *Nanotechnology* **2005**, *16*, 1234.
- (30) Verwey, E. J. W.; Overbeek, J. T. G. *Theory of the Stability of Lyophobic Colloids*; Dover Publications: New York, 1999.
- (31) Modrow, H.; Bucher, S.; Hormes, J.; Brinkmann, R.; Bonnemann, H. *J. Phys. Chem. B* **2003**, *107*, 3684.
- (32) Bucher, S.; Hormes, J.; Modrow, H.; Brinkmann, R.; Waldföner, N.; Bonnemann, H.; Beuermann, L.; Krischok, S.; Maus-Friedrichs, W.; Kempfer, V. *Surf. Sci.* **2002**, *497*, 321.
- (33) Bonnemann, H.; Brijoux, W.; Brinkmann, R.; Dinjus, E.; Joussen, T.; Korall, B. *Angew. Chem., Int. Ed. Engl.* **1991**, *30*, 1312.
- (34) Ott, L. S.; Finke, R. G. *Coord. Chem. Rev.*, submitted for publication, 2006.
- (35) Dupont, J. *J. Braz. Chem. Soc.* **2004**, *15*, 341.
- (36) Gozzo, F. C.; Santos, L. S.; Augusti, R.; Consorti, C. S.; Dupont, J.; Eberlin, M. N. *Chem.-Eur. J.* **2004**, *10*, 6187.
- (37) Hansen, J. P.; McDonald, I. R. *Theory of Simple Liquids*, 2nd ed.; Academic Press: London, 1986.
- (38) Consorti, C. S.; Suarez, P. A. Z.; de Souza, R. F.; Burrow, R. A.; Farrar, D. H.; Lough, A. J.; Loh, W.; da Silva, L. H. M.; Dupont, J. *J. Phys. Chem. B* **2005**, *109*, 4341.
- (39) Dupont, J.; Suarez, P. A. Z. *Phys. Chem. Chem. Phys.* **2006**, *8*, 2441.
- (40) Antonietti, M.; Kuang, D. B.; Smarsly, B.; Yong, Z. *Angew. Chem., Int. Ed.* **2004**, *43*, 4988.
- (41) Ott, L. S.; Cline, M. L.; Deetlefs, M.; Seddon, K. R.; Finke, R. G. *J. Am. Chem. Soc.* **2005**, *127*, 5758.
- (42) Dupont, J.; Spencer, J. *Angew. Chem., Int. Ed.* **2004**, *43*, 5296.
- (43) Bardaji, M.; Vidoni, O.; Rodriguez, A.; Amiens, C.; Chaudret, B.; Casanove, M. J.; Lecante, P. *New J. Chem.* **1997**, *21*, 1243.
- (44) Dassenoy, F.; Philippot, K.; Ould-Ely, T.; Amiens, C.; Lecante, P.; Snoeck, E.; Mossset, A.; Casanove, M. J.; Chaudret, B. *New J. Chem.* **1998**, *22*, 703.
- (45) Gomez, M.; Philippot, K.; Colliere, V.; Lecante, P.; Muller, G.; Chaudret, B. *New J. Chem.* **2003**, *27*, 114.
- (46) Gomez, S.; Erades, L.; Philippot, K.; Chaudret, B.; Colliere, V.; Balmes, O.; Bovin, J. O. *Chem. Commun.* **2001**, 1474.
- (47) Moseley, K.; Maitlis, P. M. *J. Chem. Soc., Chem. Commun.* **1971**, 982.
- (48) Suarez, P. A. Z.; Dullius, J. E. L.; Einloft, S.; DeSouza, R. F.; Dupont, J. *Polyhedron* **1996**, *15*, 1217.
- (49) Bonhote, P.; Dias, A. P.; Papageorgiou, N.; Kalyanasundaram, K.; Gratzel, M. *Inorg. Chem.* **1996**, *35*, 1168.
- (50) Cassol, C. C.; Ebeling, G.; Ferrera, B.; Dupont, J. *Adv. Synth. Catal.* **2006**, *348*, 243.
- (51) Widegren, J. A.; Aiken, J. D.; Ozkar, S.; Finke, R. G. *Chem. Mater.* **2001**, *13*, 312.
- (52) Watzky, M. A.; Finke, R. G. *J. Am. Chem. Soc.* **1997**, *119*, 10382.
- (53) Nagata, T.; Pohl, M.; Weiner, H.; Finke, R. G. *Inorg. Chem.* **1997**, *36*, 1366.
- (54) Watzky, M. A.; Finke, R. G. *Chem. Mater.* **1997**, *9*, 3083.
- (55) Carbalaj, J. R. *Short Reference Guide of The Program Fullprof*, version 3.5. Ftp://Charybde.Saclay.Cea.Fr.
- (56) Sankaran, V.; Cohen, R. E.; Cummins, C. C.; Schrock, R. R. *Macromolecules* **1991**, *24*, 6664.
- (57) Samon, J. M.; Schultz, J. M.; Hsiao, B. S. *Polymer* **2000**, *41*, 2169.
- (58) Ran, S. F.; Tong, X. H.; Fang, D. F.; Hsiao, B. S.; Chu, B.; Phillips, R. A. *Macromolecules* **2001**, *34*, 2569.
- (59) Nam, J. Y.; Kadomatsu, S.; Saito, H.; Inoue, T. *Polymer* **2002**, *43*, 2101.
- (60) Supaphol, P.; Lin, J. S. *Polymer* **2001**, *42*, 9617.
- (61) Bhattacharyya, A. R.; Ghosh, A. K.; Misra, A. *Polymer* **2001**, *42*, 9143.
- (62) Ciebien, J. F.; Cohen, R. E.; Duran, A. *Supramol. Chem.* **1998**, *5*, 31.
- (63) Ruland, W. *Colloid Polym. Sci.* **1977**, *255*, 417.
- (64) Fonseca, G. S.; Machado, G.; Teixeira, S. R.; Fecher, G. H.; Morais, J.; Alves, M. C. M. *J. Colloid Interface Sci.*, in press.
- (65) Hsiao, B. S.; Wang, Z. G.; Yeh, F. J.; Gao, Y.; Sheth, K. C. *Polymer* **1999**, *40*, 3515.
- (66) Verma, R.; Marand, H.; Hsiao, B. *Macromolecules* **1996**, *29*, 7767.
- (67) Cruz, C. S.; Stribeck, N.; Zachmann, H. G.; Calleja, F. J. B. *Macromolecules* **1991**, *24*, 5980.
- (68) Verma, R. K.; Velikov, V.; Kander, R. G.; Marand, H.; Chu, B.; Hsiao, B. S. *Polymer* **1996**, *37*, 5357.
- (69) Wagner, C. D.; Riggs, W. M.; Davis, L. E.; Moulder, J. F.; G. E., M. *Handbook of X-ray Photoelectron Spectroscopy*; Perkin-Elmer Corp.: Eden Prairie, MN, 1979.
- (70) Liu, Z.; Guo, B.; Hong, L.; Jian, H. *J. Photochem. Photobiol., A* **2005**, *172*, 81.
- (71) Zhou, Y.; Schattka, J. H.; Antonietti, M. *Nano Lett.* **2004**, *4*, 477.
- (72) McEwen, A. B.; Ngo, H. L.; LeCompte, K.; Goldman, J. L. J. *Electrochem. Soc.* **1999**, *146*, 1687.
- (73) Trewyn, B. G.; Whitman, C. M.; Lin, V. S. Y. *Nano Lett.* **2004**, *4*, 2139.
- (74) Korgel, B. A.; Fitzmaurice, D. *Phys. Rev. B* **1999**, *59*, 14191.
- (75) Hardacre, C.; Holbrey, J. D.; McMath, S. E. J.; Bowron, D. T.; Soper, A. K. *J. Chem. Phys.* **2003**, *118*, 273.
- (76) Liu, J. C.; Han, B. X.; Zhang, H. L.; Li, G. Z.; Zhang, X. G.; Wang, J.; Dong, B. Z. *Chem.-Eur. J.* **2002**, *8*, 1356.
- (77) Hornstein, B. J.; Finke, R. G. *Chem. Mater.* **2004**, *16*, 3972.
- (78) Hornstein, B. J.; Finke, R. G. *Chem. Mater.* **2004**, *16*, 139.
- (79) Besson, C.; Finney, E. E.; Finke, R. G. *J. Am. Chem. Soc.* **2005**, *127*, 8179.
- (80) Besson, C.; Finney, E. E.; Finke, R. G. *Chem. Mater.* **2005**, *17*, 4925.
- (81) Finke, R. G. In *Transition-Metal Nanoclusters*; Feldheim, D. V., Foss, C. A., Jr., Eds.; Marcel Dekker: New York, 2002; p 17.
- (82) Fonseca, G. S.; Domingos, J. B.; Nome, F.; Dupont, J. *J. Mol. Catal. A: Chem.* **2006**, *248*, 10.